ERGODIC DIVERTOR EFFECT ON LOW Z IMPURITY TRANSPORT FOR INNER WALL LIMITED PLASMAS IN TORE SUPRA

J. Hogan[*], C. De Michelis[+], P. Monier-Garbet[+], Y. Corre[+], R. Guirlet[+]

[*] *Fusion Energy Division, Oak Ridge National Laboratory, Oak Ridge, TN 37830, USA*

[+] *Association EURATOM-CEA sur la Fusion Contrôlée, CEA-Cadarache, F-13108 St-Paul-lez-Durance, France*

ABSTRACT

Observations of systematic spatial modulation of low-Z impurity radiative emissions are analysed for Tore Supra ergodic divertor discharges limited on the inner wall. Some similarities to modulations previously observed with Marfe-like conditions are observed, but significant differences are also seen in the attached cases studied here. A simulation of the modulations is made, using the 3-D edge transport code BBQ. The simulations suggest that an important role is played by charge exchange with neutral deuterium, in addition to the ergodic divertor-induced modulations of the plasma. The interpretation highlights the important role of intermediate-Z states in impurity transport processes.

1. INTRODUCTION

It is a main tokamak objective to achieve active control of the plasma edge in order to minimise the impurity influx, to improve the impurity screening efficiency, and to decrease the wall heat load by maximising the radiated power. This problem has been generally addressed by using an axi-symmetric poloidal divertor configuration (Pitcher and Stangeby, 1997), where the particle outflux is directed into a region separated from the main plasma region. An alternative solution is the ergodic divertor (ED) (Ghendrih et al, 1996), which has been extensively studied in the Tore Supra tokamak (De Michelis et al, 1995b). The ED destroys the edge plasma magnetic surfaces with a weak resonant perturbation, creating an edge layer where the field lines are stochastic, with enhanced particle and heat transport coefficients (Samain et al, 1990). Indeed, experiments have shown that the confined core plasma is efficiently screened from impurities (Breton et al, 1991), and that the radiated power is enhanced over that of non-diverted plasmas (Monier-Garbet et al,

This research was sponsored in part by the Office of Fusion Energy Sciences, U.S. Department of Energy, under contract DE-AC05-00OR22725 with Oak Ridge National Laboratory managed by UT-Battelle, LLC.

2001); moreover, 1D impurity transport simulations in ED plasmas require an increased anomalous diffusion coefficient in an outboard region roughly comparable in width to the expected ED layer (Mattioli et al, 1995), thus qualitatively confirming that the ED layer is a region with degraded confinement properties Radial profiles of impurity emission lines are used to get a better understanding of the transport modifications induced by the ED, and these can typically be obtained by inversion techniques from measured poloidal brightness distributions. However, in some experimental situations (e.g., when an outboard limiter is inserted radially ahead of the divertor modules), the poloidal impurity emission profiles exhibit a compound spatial structure [Hogan et al, 2001], showing clearly both core plasma and ED region emissions. In order to isolate and understand the ED-specific effects on transport, our approach has been to simulate the measured profiles: the axi-symmetric contribution (from the confined plasma) with a 1D radial impurity transport code, and the asymmetric component (ED region) with the BBQ 3D Monte Carlo code (Hogan et al, 1997). This approach has proven more illuminating in complex situations than the use of alternative, somewhat complicated, inversion procedures.

In this paper, we analyze the ED effect on low Z impurity emission profiles of plasmas leaning on the inner wall. In this configuration, the profile behaviour shows regular modulations for all observed peripheral impurity emission lines, clearly related to the applied ED field, and therefore should, when properly interpreted, provide information on its effect on impurity transport. Previous observations of inner-wall influenced Tore Supra ED plasmas, under detached (Marfe-like) conditions, also showed strongly modulated carbon poloidal profiles, varying coherently with the safety factor q, but only for $\Delta n=1$ emission lines (n being the transition principal quantum number), for which the excitation cross section is T_e-dependent in the temperature range of interest (De Michelis et al, 1995a). This was interpreted as a consequence of the T_e modulations due to the connections provided by the ED to the hot core region. The new observations discussed here give rise to a qualitatively different behaviour; the purpose of this paper is to provide a common basis for interpretation of the measured signals, and thus permit future dedicated analysis of transport behaviour.

We first describe the experimental conditions for the measurements (section 2). Section 3 describes the models used to create the simulations of the impurity emission signals, section 4 the signal simulation results, and section 5 presents the interpretation, which we obtain.

2. EXPERIMENTAL

2.1. Typical plasma

All the plasmas used in this study were in the Ergodic Divertor (ED) configuration (Ghendrih et al, 1996). In the ED configuration, the current flowing in the divertor coils (I_{ED}) generates a

resonant perturbing magnetic field, which, at the maximum ergodic divertor current (I_{ED}= 45 kA), has an intensity $<|\delta B_r|^2>^{1/2} / B_t \sim 10^{-3}$. The effect of this perturbation is to open the magnetic flux surfaces in the plasma periphery, thus connecting the edge field lines to the divertor neutraliser plates (NP), located inside the ED current loops (Ghendrih et al, 1996).

To study the ED effects on inner wall limited plasmas, we have performed a few shots with the procedure illustrated in Figure 1 (I_{ED} = 40 kA during the entire shot, nearly at its maximum value). A large initial plasma, limited by both the outboard ED modules and the inner wall, was moved inwards at 3.5 s, to become only inner wall limited, by decreasing the major radius (R); at approximately 5 s, the plasma radius (a) also started to decrease; at the same time, the plasma current (I_p) also decreased slowly. The electron density N_e slowly increased during this phase, because of increased inner wall recycling (there was no deuterium gas injection, apart from the initial pre-fill). The D_α inner wall lines of sight showed a strong recycling increase, starting at 3.5 s, while at the same time recycling on the neutralisers decreased, the neutraliser Dα signal being negligible after 6 s. The effective charge Z_{eff} initially increases (as does the OVIII Lyman-α signal); after an accidental C and O injection between approximately 5 and 6 s, Z_{eff} decreases because of the increasing N_e. It must be noted here that past ED experiments have shown T_e modulations in the ED layer, due to the random field line connections provided by the ED to the hot core and to the cold plasma facing components (Becoulet et al, 1999).

2.2. Spectroscopy

Impurities were monitored by two far VUV spectrometers. The first one, an absolutely calibrated extreme grazing incidence (1.5°) far VUV (1 - 30 nm) duochromator, provided monitoring of the CVI and OVIII Lyman-α lines, thus permitting to evaluate the respective contribution of C and O to the Z_{eff} value (deduced from the visible bremsstrahlung emission). Carbon and oxygen are the only impurities present in these plasmas, a consequence of the all carbon plasma-facing components in Tore Supra. The second spectrometer, a grazing incidence (5°) far VUV (5 - 15 nm) duochromator, used a vibrating grazing incidence gold coated mirror to provide poloidal profiles of the plasma lower half, with a spatial resolution of 0.03 m (Breton et al, 1979). This second duochromator has two multi-anode, microchannel plate detectors (spectral resolution 0.13 nm), thus permitting to monitor simultaneously the profiles of several emission lines (De Michelis et al, 1993). Figure 2 shows schematically the experimental set-up of this second

duochromator, together with an example of a 'normal' profile (i.e., from a homogeneous emitting peripheral shell) for the OV 63.0 nm line.

2.3. Experimental observations

For these inner-wall limited plasmas, modulations appear on all observed impurity line profiles at 4.5 s, their depth increasing with time; they are stronger at approximately 9 s, when N_e and the inner wall $D\alpha$ signal are at their maximum. An example is shown in Figure 3 for three peripheral emission lines: CIII 97.7 nm (a $\Delta n=0$ transition), CIV 31.2 nm ($\Delta n=1$, observed in the second order), and OV 63.0 nm ($\Delta n=0$); note that these three profiles have been taken simultaneously. The modulations are sharper and more irregular for the CIII 97.7 nm line, which is the more peripheral of the three observed lines (C^{2+} ionisation potential, E_i = 48 eV); they become smoother and more regular as the ionisation potential of the emitting ion increases (E_i = 64 eV for C^{3+}, and 114 eV for O^{4+}). This is probably a consequence of the fact that low ionisation potential ions have no time to become poloidally and toroidally uniform, and their emission still partly reflects the location of the plasma-surface interaction. Among the three observed emission lines, only CIV 31.2 nm originates from a $\Delta n=1$ transition, for which the excitation cross section is T_e-dependent in the range of temperature of interest; the other two emission lines originate from a $\Delta n=0$ transition, for which the excitation cross section is approximately independent of T_e in the range of temperature of interest. The number of modulations increases as the plasma current I_p decreases (and the safety factor, $q = 5a^2B_t/I_pR$, increases); Figure 4 shows this effect for a sequence of profiles for the OV 63.0 nm line. Figure 5 summarises this data, showing the variation of the number of modulations with I_p as q varies from 2.6 to 3.2.

A survey of ED plasmas, limited outboard either by the ED modules or by an inserted poloidal limiter, shows that modulations in such cases appear only when the distance Δ_{IW} between the last closed flux surface (calculated without ergodic divertor current, I_{ED} = 0) and the inner wall is of the order of or less than 0.06 m (in most experiments it is at least 0.1 m); however, inner wall limited plasmas produce the strongest modulations. Again, modulations are observed on both $\Delta n=1$ and $\Delta n=0$ transitions of peripheral C and O ions; moreover, when heavier extrinsic impurities are injected (such as Neon), they are observed also for ions with a relatively large ionisation potential,

having a radial position at the inner limit of the ED layer. Figure 6 shows the profiles of three Neon lines, NeVII 10.6 nm (a $\Delta n=1$ transition), NeVIII 9.8 nm ($\Delta n=1$), and NeVIII 77.0 nm ($\Delta n=0$); the modulations are clearly attenuated in passing from NeVII (E_i = 207 eV for Ne^{6+}) to NeVIII (E_i = 239 eV for Ne^{7+}), and apparently they do not exist at all on the NeVIII $\Delta n=0$ line. A confirmation that these ions exist at the inner limit of the ED layer comes from their emission profiles, showing that the position of the peripheral peak, the homogeneous radiating shell, is practically the same with and without I_{ED}.

The inner-wall case observations described above are clearly at variance with those reported earlier (De Michelis et al, 1995a). In that case, the plasma (having the outboard limiter positioned ahead of the ED modules) was not moved inwards, but the electron density was increased by a strong deuterium gas puff, the radiation maximum eventually swinging from outwards to inwards (the plasma then showing an inner wall Marfe-like structure). In the situation described here, the plasma is moved inwards without trying to increase the density (which increases somewhat because of the increased recycling), and remains attached to the inner wall. In summary, in the present case, with inner wall attached plasma conditions, the following new features are observed:

(1) for the modulations to occur, the clearance between the last closed flux surface and the inner wall (Δ_{IW}), calculated without ergodic divertor current (I_{ED} =0), must be less than 0.06m;

(2) the modulations are observed on emission lines originating from both $\Delta n=0$ and $\Delta n=1$ transitions (therefore, the effect of the T_e modulations on the excitation cross sections cannot explain both cases);

(3) the modulations do not depend as sensitively on the radial position of the emitting impurity; and

(4) modulations are seen on emission from ions with a relatively large ionisation potential (Ne^{6+} and Ne^{7+}), having a radial position at the inner limit of the ED layer.

The previous interpretation of the observations in Marfe-like conditions (De Michelis et al, 1995a) requires therefore an extension to include these new conditions.

3. SIMULATION MODELS

To attempt an interpretation, modelling of the impurity transport behaviour in the ED plasmas is made with a 3-D impurity transport code (BBQ). The modelling requires background plasma parameters, as they are modified by the ED. Given this, the simulation is used to construct the emission profiles for comparison with the measurements. Since the study suggests that charge-exchange processes may play a role, a deuterium version of the 3-D BBQ code is used to calculate

the neutral D spatial distribution in the observation region. This section is devoted to a description of these elements of the simulation.

3.1 BBQ code

BBQ is a 3-D Monte Carlo impurity transport code for the scrape-off layer and plasma edge region (Hogan et al, 1997, Giannella et al, 2001). The code follows the transport of trace impurity particles, assuming a known 3-D background plasma spatial distribution (N_e, T_e, and **B**), as the impurities evolve from emission as neutrals at the plasma-facing components through the various ionisation stages. The density of the observed ion, as well as the emission rate of the observed radiation, is calculated for each point in the calculation region. The predicted emission signal is integrated over the individual viewing chords of the duochromator for comparison with data.

Particle generation rates from the plasma-facing components for carbon are calculated from physical sputtering rates evaluated for the complex inner wall geometry (Hogan, 1998), assuming a Thomson energy distribution for the sputtered carbon neutrals. Oxygen generation rates are based on a modification of the carbon rates. For neon, TRIM reflection probabilities and energies for neon on carbon (Eckstein et al, 1998) are used for the TRIM-calculated fraction of directly reflected particles, and thermal emission is assumed for the remainder.

Atomic data for the impurity transport calculations is taken from Phaneuf et al (1987) for carbon and oxygen, and from the ADAS database (corrected by R. Dux) for neon (Summers, 1994). Emission rates for neon $\Delta n=0$ and $\Delta n=1$ lines are those calculated by Mattioli et al (1999). Rates based on the empirical formulae of Mewe et al (1980) for $\Delta n=0$ lines of Ne^{3+} and Ne^{4+} ions have been communicated by Isler (2000). A detailed model for carbon and oxygen charge exchange processes (Maggi et al, 2000) has been incorporated in BBQ.

3.2 Background plasma model

An ED background plasma model, originally developed to treat the ED neutraliser plate region (Giannella at al, 2001), has been extended to calculate the background plasma parameter (N_e, T_e, and **B**) distributions in an annular region bounded by the inner and outer limits of the ergodic zone ($0.65 < r < 0.8$ m) and by the poloidal ($0 < \theta < 60°$) and toroidal ($-20° < \phi < 20°$) angular limits of the region viewed by the duochromator. The background plasma parameters (3-D spatial distributions of N_e, T_e, and magnetic field **B**) are calculated in this annular region with a suitably modified version of the MASTOC mapping procedures (Nguyen et al, 1997), developed by Giannella et al (2001). Each of $4*10^5$ points in the computation volume is first mapped to a point on the annular bounding surface. In the next step, a grid with reduced resolution is produced on the

bounding surfaces and the MASTOC code is used to trace the path of field lines emanating from each point on the bounding surfaces to determine the maximum inward penetration into the core plasma (ρ_{min}) of field lines which originate there. The result of this step is to provide a distribution of ρ_{min} on the bounding surface and, thus, via the first map, to each point in the computation volume. The final step is to associate a value of T_e with the values of ρ_{min} on the bounding surface, based on the assumption of rapid parallel electron thermal transport. A linear relation $T_e = - k (\rho_{min}-\rho_{local})$ is used. Unlike the divertor neutraliser case described by Giannella et al (2001), where local Langmuir probe T_e measurements were available to calibrate the T_e map, only the relative variation of the ED-induced modulations can be used, using the flux-surface average T_e values as a normalisation. Figure 7 shows the results of the T_e mapping procedure on the bounding surfaces. Distributions are shown of values of the minimum radius in the hot core which is reached by field lines traced from the bounding surfaces. Distributions on the six bounding surfaces of the simulation volume are shown, for values of constant normalised radius ρ (inner and outer), poloidal angle θ (minumum and maximum) and toroidal angle ϕ (minumum and maximum). The sections at constant toroidal angle ϕ (showing the $\rho-\theta$ plane), exhibit the periodic poloidal oscillations in the T_e values induced by the ED. The sections at constant ρ (showing the $\theta-\phi$ plane) at the innermost radius considered and on the exterior, show the attenuation of the ED perturbation in this direction. Finally, the sections at constant θ ($\rho-\phi$ plane) show the variation across the line of sight of the duochromator volume.

3.3 Deuterium simulation

Previous Tore Supra outer limiter particle exhaust studies have shown that outboard pumping was ineffective unless $\Delta_{IW} \geq 0.1$m, indicating a strong plasma interaction with the inner wall when $\Delta_{IW} < 0.1$m (Mioduszewski et al, 1995). Comparison of inner wall heat fluxes with observation also found large scrape-off-layer decay lengths (Seigneur et al, 1993). Significant inner wall deuterium recycling thus occurs for $\Delta_{IW} < 0.1$m, such that the effect of charge exchange with neutral deuterium on impurity emission profiles could be important. Charge exchange of deuterium with low Z impurities has been known for some time to affect the ionisation balance (Hogan, 1982, 1984). Although charge exchange rates are not available for the entire suite of ion charge states for neon, magnitudes are expected to be similar to the carbon and oxygen rates for similar ions in the

iso-electronic sequence. The details of inner wall construction (faceted graphite blocks, tangent to the plasma minor radius at only one point) provide another possible source of periodic modulation of impurity emission, through modulation of the charge exchange rates. Thus, since modulations are observed only when first-wall clearance $\Delta_{IW} < 0.06$m, neutral deuterium density spatial distributions are also required in this region.

The deuterium version of BBQ is used to calculate D and D_2 transport, accounting for ionisation, recombination, dissociation and dissociative ionisation. The same background plasma model, discussed above, is used with the deuterium version of BBQ. Calculations with the MASTOC field line following code show that the poloidal distribution of T_e at the inner wall should also be modulated when $I_{ED} > 0$ (Figure 8); poloidal T_e modulations have been experimentally observed for outboard limited plasmas (Becoulet et al, 1999). Thus, the incident D^+ flux on the inner wall is modulated via the dependence of the sheath potential on T_e. This produces an ED-modulated deuterium density reflux from the plasma-facing surface, because of the T_e dependence of the particle energy for the energetically reflected fraction of D neutrals. In addition, the remainder, which consists of thermally emitted D_2 molecules, will also exhibit modulations, because the more intense influx produces locally modulated saturation. The 3-D neutral transport code self-consistently calculates the attenuation and dispersion of this wall modulation through the neutral transport processes: extinction of the neutral atoms by ionisation, production and dispersal of energetic Franck-Condon atoms from the D_2 molecules, and atom momentum scattering by charge exchange with background D^+.

Another consideration is that T_e is reduced in the ergodic zone, increasing the ionisation path length for recycled deuterium neutrals. Ergodic zone T_e profiles similar to those measured in outboard limited plasmas for I_{ED}=35kA (Becoulet et al, 2000) are used in the simulation. The radial deuterium atom density (Figure 9a) and the neutral density averaged over the duochromator sight lines (Figure 9b), resulting from the BBQ deuterium model calculation, show (1) the differences introduced in using the ED T_e profiles (Fig. 9a) and (2) the interference effects between the modulation due to faceted tiles, which is present even when I_{ED}=0, and the independent systematic variation of modulation with I_{ED}. (Fig. 9b, cases with and without ED). However, even in cases where this leads to an incoherent poloidal modulation, a strong neutral deuterium density is present in the ergodic zone.

3.4 Signal simulation

Given the background plasma model, and the generated fluxes of neutral impurities, the density of all species, $N_{Zk}(\rho,\theta,\phi)$, is calculated by BBQ. With the value of $T_e(\rho,\theta,\phi)$ given by the background plasma model, and emission coefficients for the line being modelled, a prediction of the expected poloidal emission signal is obtained. Using the radial profiles of the emitting ions in all charge states from the 1D radial impurity transport code MIST (Hulse, 1983), the associated duochromator signal is calculated with the actual geometry (Figure 2), using the excitation rates for ions described in section 3.1.

4. PROFILE SIMULATION

Using the BBQ results both for impurity ions and for deuterium, the simulated poloidal emission profiles are thus calculated for the ions of interest. Figure 10 (a, b, c) shows the simulated profiles for the CIV 31.2 nm, OV 63.0 nm, and NeVIII 9.8 nm lines, without ($N_{D0}=0$) and with ($N_{D0}=10^{17}$ m^{-3} and 10^{18} m^{-3}) charge-exchange. As discussed above, even without charge-exchange, there is some modulation of the profiles, due to the faceted carbon tiles. Because of the assumptions required in the analysis, due to lack of local 3-D T_e measurements to calibrate the MASTOC T_e map, only qualitative trends can be compared. However, there is a reasonable and encouraging similarity between the simulation results and the corresponding measured profile behaviour, shown in Figures 3 and 6. Note that the modulation of the signal changes qualitatively as the CX effect is introduced (case with $N_{D0}=0$ versus case with $N_{D0}=10^{17}$ m^{-3}) while the amplitude is increased with mainly fixed modulation as neutral density is increased from $N_{D0}=10^{17}$ m^{-3} to $N_{D0}=10^{18}$ m^{-3}. Thus there appears to be a threshold level in the simulation required for the CX effect to determine the ion charge state distribution, and higher values of neutral density amplify this charge state distribution. Note that, although 10^{18} m^{-3} seems a large value for the peripheral neutral deuterium density, values of this order of magnitude have been measured for ED outboard limited plasmas, just in front of the neutralisers (Escarguel et al, 2001). Figure 11 shows a simulation of the variation of the number of modulations with I_p for the NeVIII 9.8 nm line. The background 3-D distributions of T_e and N_{D0} for these cases are modulated using the relation between poloidal mode number and I_p, discussed by De Michelis et al (1995a). Again, the qualitative trend of systematic increase of modulation number with increasing q is reasonably consistent between the simulation and the measurement.

5. CONCLUSIONS

Reviewing the novel observed features (section 2 above), in comparison with previous inner wall cases with Marfe-like conditions, an interpretation based on the simulation can be attempted:

1. For the modulations to occur, the clearance between the last closed flux surface and the inner wall (Δ_{IW}, calculated without ergodic divertor current), must be less than 0.06m. Simulation suggests that the profile modulations are indeed directly related to modulations of T_e, but also to the consequent modulation of the large neutral D outflux, resulting in an important modulated neutral D density in the ergodic zone precisely under these conditions.

2. The modulations are observed on emission lines originating from both $\Delta n=0$ and $\Delta n=1$ transitions. Therefore, the effect of the T_e modulations on the excitation cross sections cannot explain both cases. However, T_e modulations also modulate, through the sheath potential, the D^+ outflux; as a consequence, neutral charge exchange modulates the recombination rate, and therefore the ionisation stage. In addition, of course, there is an important effect on modulation of ions with a given charge precisely because of local T_e modulation.

3. The modulations do not depend as sensitively on the radial position of the emitting impurity, since T_e in the ergodic zone is relatively flat in cases with ED.

4. Modulations are seen on emission from ions with a relatively large ionisation potential (Ne^{6+} and Ne^{7+}), having a radial position at the inner limit of the ED layer, because charge exchange increases the apparent ionisation potential of impurity ions, leading to the appearance of NeVII and NeVIII emission.

The Chirikov island overlap parameter in the ED layer, which measures the degree of stochasticity of field line diffusion induced by the ED, decreases steadily when going radially inwards. The largest quasilinear field line diffusion coefficients should thus occur nearest the edge, and diminish radially inward. Furthermore, the poloidal mode number of the perturbation also decreases when going radially inwards (as local q decreases). Thus, from the ED effect alone, one would expect that the number of modulations be larger for the emission profiles of lower ionisation potential ions (i.e., larger at greater ion minor radial location). As this is clearly not the case, a more economical interpretation is that the charge-exchange-induced modulation in the recombination rates, which must play a role for inner-wall influenced conditions, has the effect of modulating the profiles; the observed modulations actually originate at the plasma surface interaction region, and then propagate inwards due to the long deuterium ionisation length. While no direct proof for the charge exchange hypothesis can be advanced, given existing data, the qualitative results of the simulations discussed here strongly support it.

The simulation results allow a possible resolution of some of the paradoxes suggested by comparison with previous Marfe-like results, and thus suggest a path forward for analysing the ED-induced effects on transport. More detailed transport analysis to extract ED-specific effects on transport in such cases must thus incorporate detailed spatial information on neutral deuterium behaviour along with the detailed ion distribution and background plasma data. A direct line-by-line fitting simulation is thus feasible, even in this complex situation, and can provide information about the underlying transport.

ACKNOWLEDGEMENTS

This work could not have been possible without the dedication of the Tore Supra operation group, as well as of all the members of the ED Task Force, under the co-ordination of Ph. Ghendrih. We also thank Ph. Ghendrih and J. Gunn for use of the MASTOC-based mapping programs which we used as a starting point for this application.

REFERENCES

BECOULET M., CAPES H., GHENDRIH Ph., GROSMAN A., GUNN J., HOANG J.T., SEGUI J.L. and ZABIEGO M., 2000, Contrib. Plasma Phys. **40** 251

BECOULET M., GHENDRIH Ph., CAPES H. and GROSMAN A., 1999, Controlled Fusion and Plasma Physics (Proc. 26th Eur. Conf. Maastricht, 1999), European Physical Society, Geneva, **23J** 989

BRETON C., DE MICHELIS C., FINKENTHAL M. and MATTIOLI M., 1979, J. Phys. E: Sci. Instrum. **12** 894

BRETON C., DE MICHELIS C., MATTIOLI M., MONIER-GARBET P., AGOSTINI E., FALL T., HESS W., LASALLE J., EVANS T.E., GROSMAN A., GHENDRIH Ph., PECQUET A.L., POUTCHY L., SAMAIN A. and VALLET J.C., 1991, Nucl. Fusion **31** 1774

DE MICHELIS C., GHENDRIH Ph., GUIRLET R., HESS W., MATTIOLI M., MONIER-GARBET P., GROSMAN A., NGUYEN F. and VALLET J.C., 1995a, Plasma Phys. Control. Fusion **37** 505

DE MICHELIS C., GROSMAN A., GARBET X., GHENDRIH Ph., GONICHE M., HESS W.R., LAVIRON C., LOARER T., MATTIOLI M., MONIER-GARBET P., SAOUTIC B, CLAIRET F., GUILHEM D., GUIRLET R., HOANG T. and LASALLE J., 1995b, Nucl. Fusion **35** 1133

DE MICHELIS C., MATTIOLI M., MONIER-GARBET P., VIDAL J.C. and HECQ W., 1993, Meas. Sci. Technol. **4** 109

ECKSTEIN W., 1998, Garching IPP-Report 9/117

ESCARGUEL A., GUIRLET R., AZEROUAL A., PEGOURIE B., GUNN J., LOARER T., CAPES H., CORRE Y., DE MICHELIS C., GODBERT-MOURET L., KOUBITI M., MATTIOLI M. and STAMM R., 2001, J. Nucl. Mater. **290-293**

GHENDRIH Ph., GROSMAN A. and CAPES H., 1996, Plasma Phys. Control. Fusion **38** 1653

GIANNELLA R., CORRE Y., HOGAN J.T., GHENDRIH Ph., GUIRLET R. and GUNN J., 2001, Plasma Phys. Control. Fusion **43** 271

HOGAN J., 1982 in "Physics of Electronic and Ionic Collisions", XII ICPEAC (International Conference on Physics of Electronic and Atomic Collisions), S. Datz, Ed. North-Holland, Amsterdam, 769

HOGAN J., 1984 in "Applied Atomic Collision Physics", Vol. 2, C.F. Barnett, M.F.A. Harrison, Eds., Academic Press, Orlando, 114

HOGAN J.T., KLEPPER C.C., HARRIS J.H., MIODUSZEWSKI P., ISLER R.C., CHATELIER M., DE MICHELIS C., GONICHE M., HESS W.R., MATTIOLI M., MANDL W., MITTEAU R., MONIER-GARBET P., SCHLOSSER J., TORE SUPRA TEAM, TOBIN S.J., PHILIPPS V., KOEGLER U. and WINTER J., 1997, 16th Intern. Conf. Plasma Physics Controlled Nuclear Fusion Research (Montreal, 1996), IAEA: Vienna, **2** 625

HOGAN J., GUILHEM D., CORDIER, J-J., SKINNER C., MUELLER D. and BASHORE D. Fusion Technol. **34** (1998) 454

HOGAN J., DE MICHELIS C., MONIER-GARBET P., BECOULET M., BUSH C., GHENDRIH PH., GUIRLET R., HESS W., MATTIOLI M., AND VALLET J-C., 2001, J. Nucl. Mater. **290-293** 628

HULSE R.A., 1983, Fusion Technol. **3** 259

ISLER R.C., 2000, private communication

MAGGI, C.F., HORTON, L.D. and SUMMERS H.P., 2000, Plasma Phys. Control. Fusion, **42** 669

MATTIOLI M., DE MICHELIS C. and MONIER-GARBET P., 1995, Nucl. Fusion **35** 807

MATTIOLI M., FOURNIER K., CARRARO L., DEMICHELIS C., MONIER-GARBET P., PIUATTI M.E., SATTIN F., SCARIN P. and VALISA M., Phys. Rev. E **60** (99) 4760

MEWE R., SCHRIJVER J. and SYLWESTER J., 1980, Astron. Astrophys., **87** 55

MIODUSZEWSKI P., HOGAN J., OWEN L., MAINGI R., LEE D.K., HILLIS D. L., KLEPPER C. C., MENON M. M., THOMAS C. E., JR., UCKAN T., WADE M., CHATELIER M., GRISOLIA C., GHENDRIH Ph., GROSMAN A., HUTTER T., LOARER T., PEGOURIE B., MAHDAVI A. and SCHAFFER M., 1995, J. Nucl. Mater. **220** 91

MONIER-GARBET P., DE MICHELIS C., GHENDRIH Ph, GRISOLIA C., GUIRLET R., GUNN J., LOARER T., BUSH C., CLEMENT C., CORRE Y., COSTANZO L., HOGAN J.T., SCHUNKE B. and VALLET J.C., 2001, J. Nucl. Mater. **290-293** 925

NGUYEN F., GHENDRIH Ph. and GROSMAN A., 1997, Nucl. Fusion **37** 743

PHANEUF R.A., JANEV R.K. and PINDZOLA M.S., 1987, Collisions of carbon and oxygen ions with electrons, H, H2 and He, ORNL-6090, Oak Ridge National Laboratory, Oak Ridge, TN, USA

PITCHER C.S. and STANGEBY P.C., 1997, Plasma Phys. Control. Fusion **39** 779

SAMAIN A., BLENSKI T., GHENDRIH Ph. and GROSMAN A., 1990, Contr. Plasma Phys. **30** 157

SEIGNEUR, A., GUILHEM, D., HOGAN, J., DE MICHELIS C., GHENDRIH Ph., GONICHE M., GROSMAN A., GUIRLET R., HESS W., LASALLE J., VALTER J. and SAMAIN A., 1993, Controlled Fusion and Plasma Physics (Proc. 20th Eur. Conf. Lisboa, 1993), European Physical Society, Geneva, **17C** 603

SUMMERS H P, 1994, Atomic Data and Analysis Structure (ADAS), Report JET-IR(94)06 JET Joint Undertaking, Abingdon (England); ADAS User Manual, version 2.2 2000 *http://patiala.phys.strath.ac.uk/ adas/*

FIGURE CAPTIONS

Fig. 1 - Operational scenario for inner wall limited plasmas; time evolution of: plasma current I_p, volume averaged electron density $<N_e>$, effective charge Z_{eff}, major plasma radius R, and minor plasma radius a.

Fig. 2 - Schematic view of the duochromator set-up (top with the plasma-facing components, the duochromator lines of sight and the vibrating mirror geometry. At bottom, (b), an example ia shown of a 'normal' poloidal profile of the OV 63.0 nm emission line ('normal' meaning that it is produced by a poloidally homogeneous peripheral radiating shell).

Fig. 3 - Experimental inner wall poloidal duochromator profiles of oxygen (OV 63.0 nm, top), and carbon (CIV 31.2 nm, middle, and CIII 97.7 nm, bottom). Δn is the difference of the principal quantum numbers of the transition upper and lower levels.

Fig. 4 - Four OV 63.0 nm line emission profiles with different number of modulations as the plasma current I_p decreases.

Fig. 5 - Variation of number of modulations in the OV 63.0 nm line profiles with I_p (i.e., q), for I_{ED}=40 kA.

Fig. 6 - Experimental inner wall poloidal duochromator profiles of two neon ions (NeVII 10.6 nm, top; NeVIII 9.8 nm, middle; and NeVIII 77.0 nm, bottom). Δn is the difference of the principal quantum numbers of the transition upper and lower levels.

Fig. 7 - ρ_{min} distributions on boundary surfaces of BBQ simulation volume, from MASTOC based mapping; ρ_{min} values are then related to T_e (see text)

Fig. 8 - MASTOC calculation of the poloidal and toroidal distribution of the minimum minor radius linked to the observation volume (r_{min}, thus T_e and D^+ flux) at the inner wall location.

Fig. 9 - (a): BBQ calculation of radial neutral deuterium density with and without edge T_e profile due to ED; (b): neutral density averaged over duochromator sight lines with no ED and with a background plasma with 9 poloidal modulations in the T_e profile.

Fig. 10 - Simulated poloidal profiles of CIV 31.2 nm (top), OV 63.0 nm (middle), and NeVIII 9.8 nm lines for three cases: N_{D0}= 0, 10^{17} m^{-3} and 10^{18} m^{-3}.

Fig. 11 - Simulated dependence of modulation number with q for the NeVIII 9.8 nm line profile, for three values of the plasma current I_p (I_{ED}=45 kA) with N_{D0}= 10^{17} m^{-3}

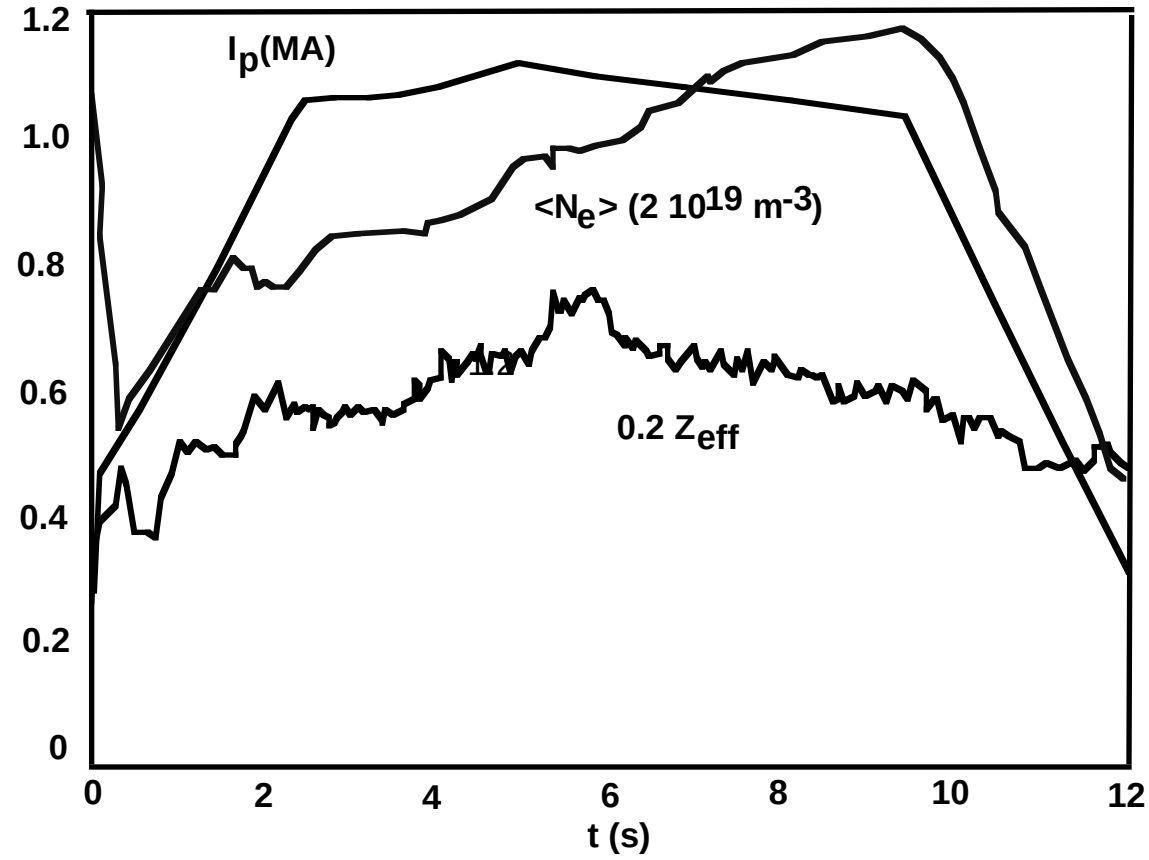
1.2
1.0
0.8
0.6
0.4
0.2
0
I_p(MA)
<N_e> (2 10^{19} m^{-3})
P_{N2}
0.2 Z_{eff}
0
2
4
6
8
10
12
t (s)

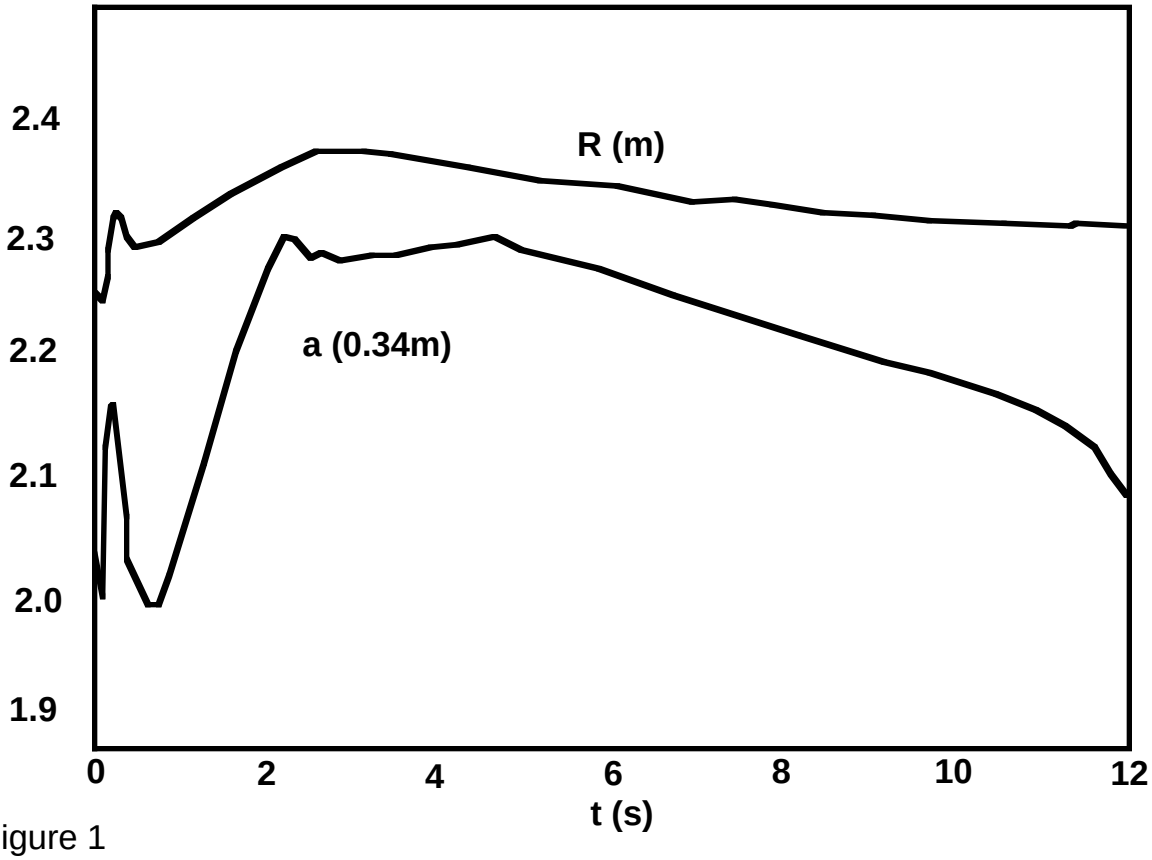
2.4
2.3
2.2
2.1
2.0
1.9
R (m)
a (0.34m)
0
2
4
6
8
10
12
t (s)

Figure 1

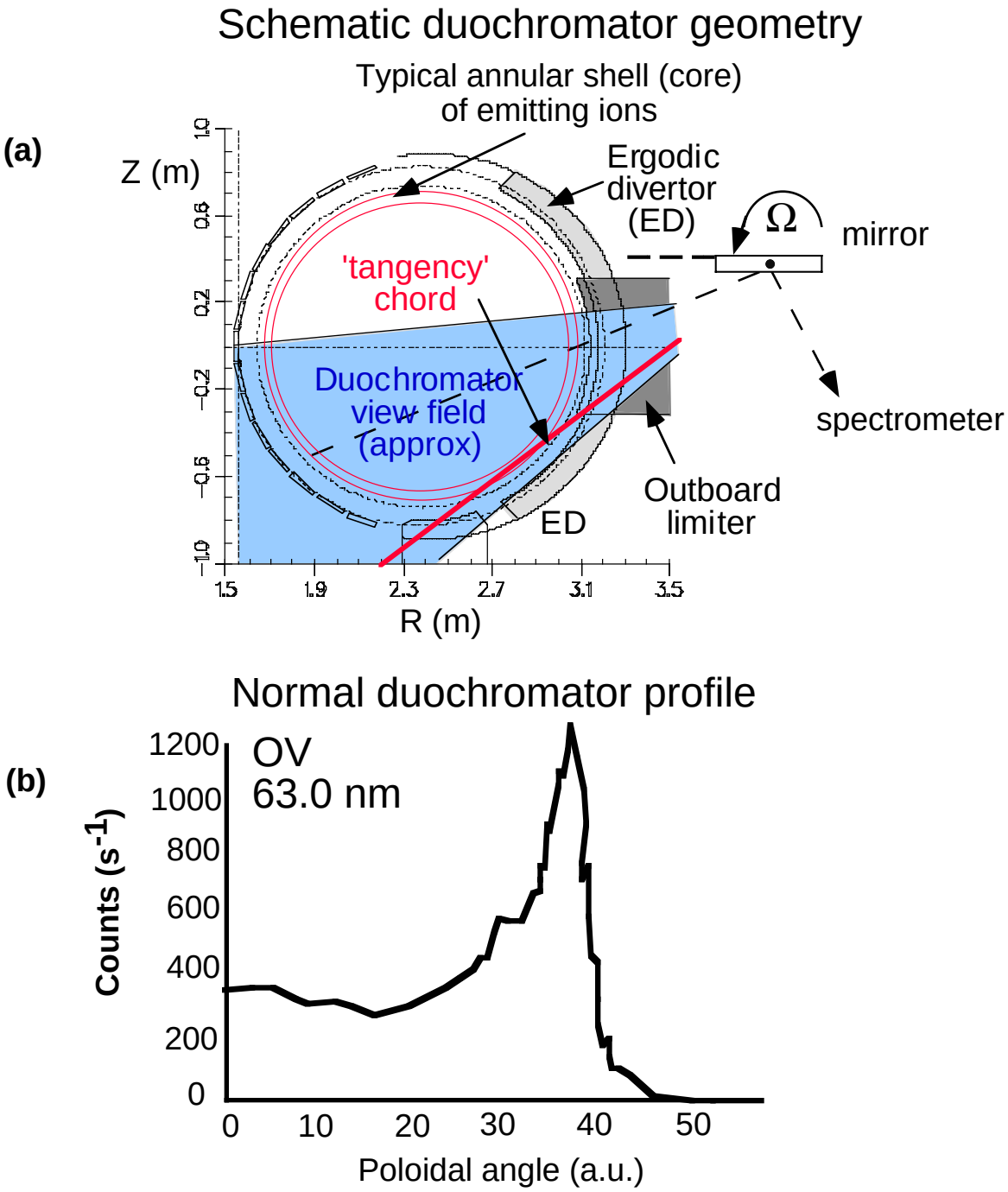
(a)
Schematic duochromator geometry
Typical annular shell (core)
of emitting ions
Ergodic
divertor
(ED)
Ω
mirror
'tangency'
chord
Duochromator
view field
(approx)
spectrometer
Outboard
limiter
ED
Z (m)
R (m)
1.0
0.6
0.2
-0.2
-0.6
-1.0
1.5
1.9
2.3
2.7
3.1
3.5
(b)
Normal duochromator profile
OV
63.0 nm
Counts (s-1)
1200
1000
800
600
400
200
0
0
10
20
30
40
50
Poloidal angle (a.u.)

Figure 2

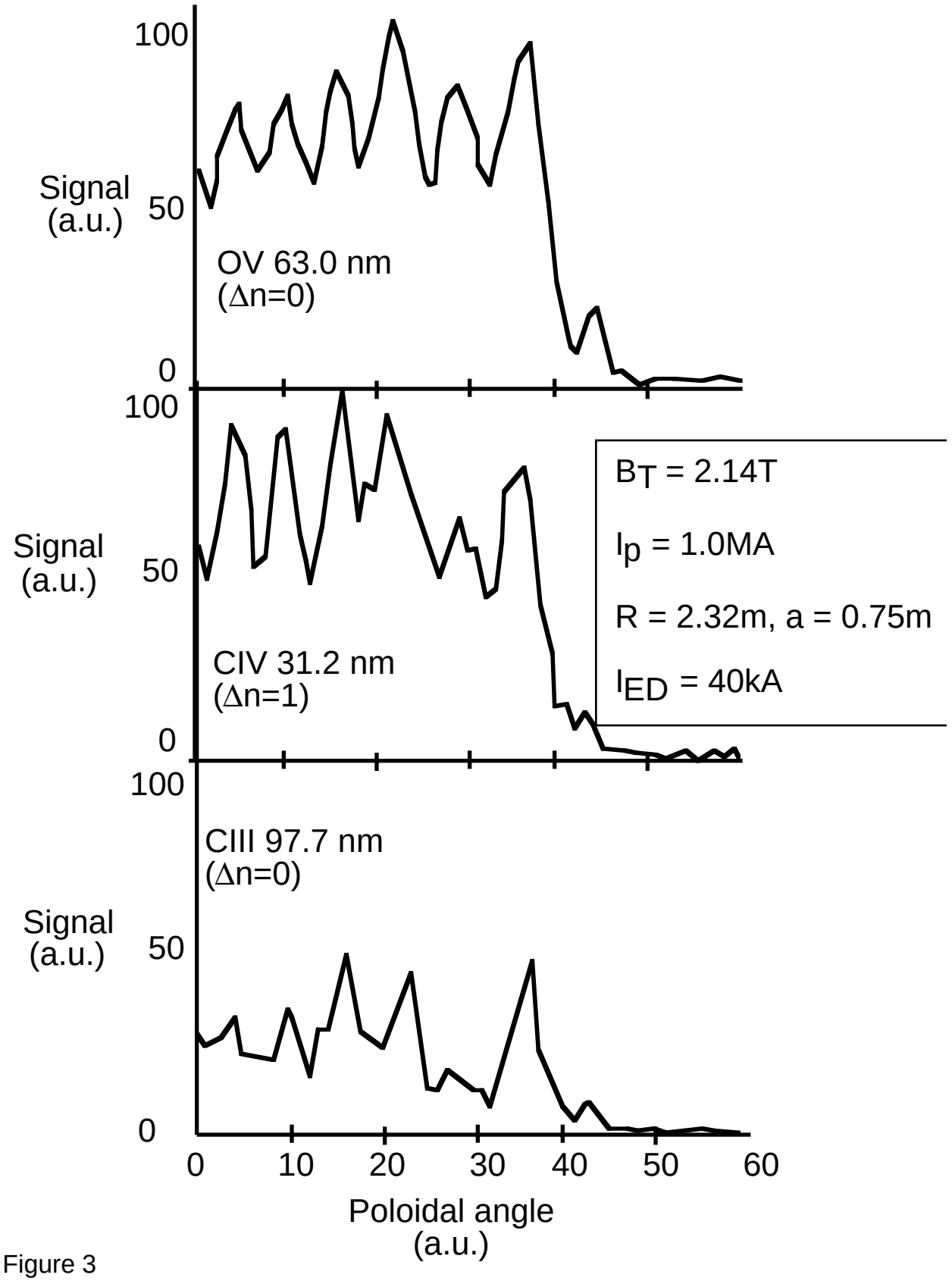
100
Signal
(a.u.)
50
OV 63.0 nm
(Δn=0)
0
100
Signal
(a.u.)
50
CIV 31.2 nm
(Δn=1)
0
B_T = 2.14T
I_p = 1.0MA
R = 2.32m, a = 0.75m
I_{ED} = 40kA
100
CIII 97.7 nm
(Δn=0)
Signal
(a.u.)
50
0
0
10
20
30
40
50
60
Poloidal angle
(a.u.)

Figure 3

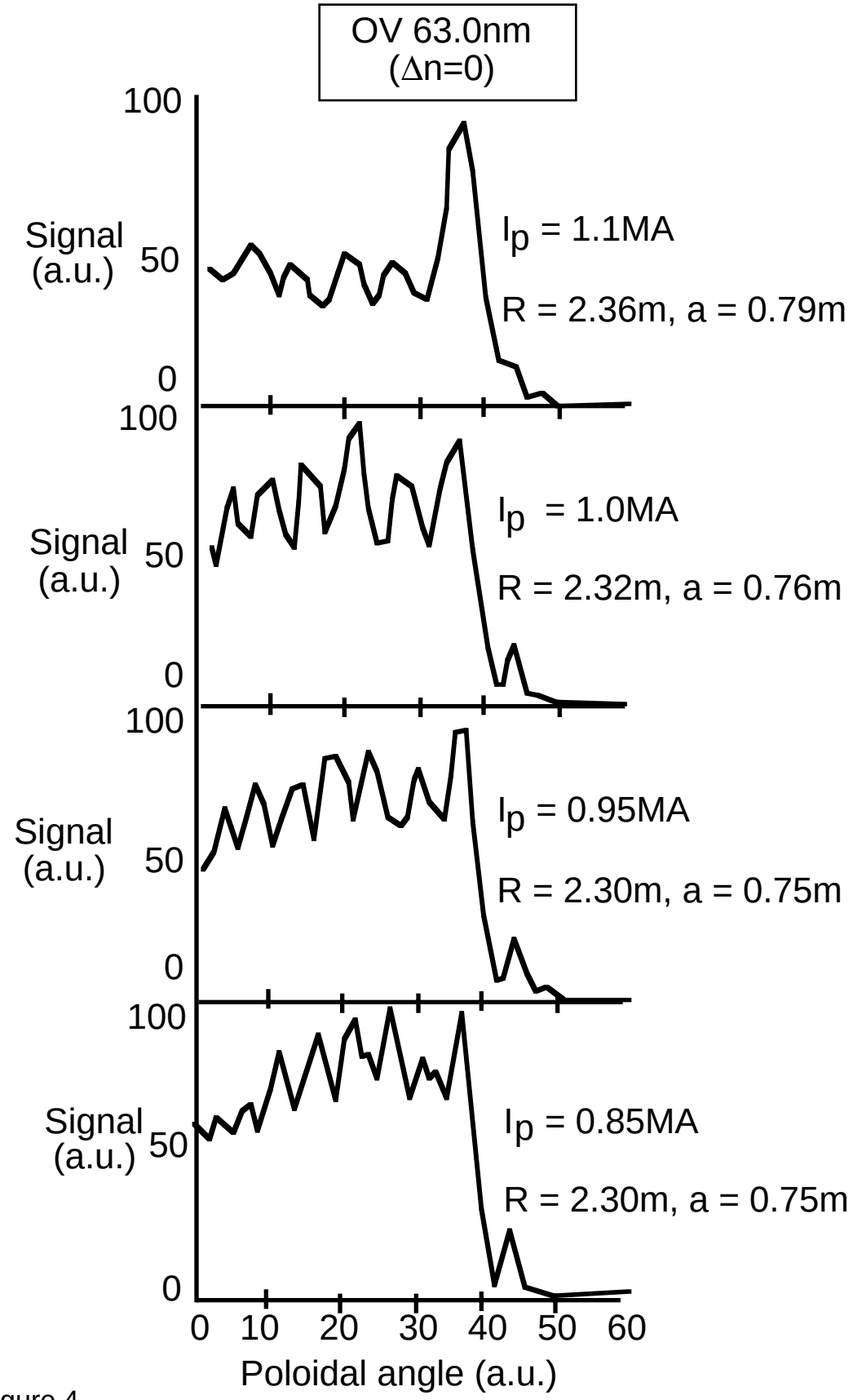
OV 63.0nm
(Δn=0)
100
Signal
(a.u.)
50
0
I_p = 1.1MA
R = 2.36m, a = 0.79m
100
Signal
(a.u.)
50
0
I_p = 1.0MA
R = 2.32m, a = 0.76m
100
Signal
(a.u.)
50
0
I_p = 0.95MA
R = 2.30m, a = 0.75m
100
Signal
(a.u.)
50
0
I_p = 0.85MA
R = 2.30m, a = 0.75m
0 10 20 30 40 50 60
Poloidal angle (a.u.)

Figure 4

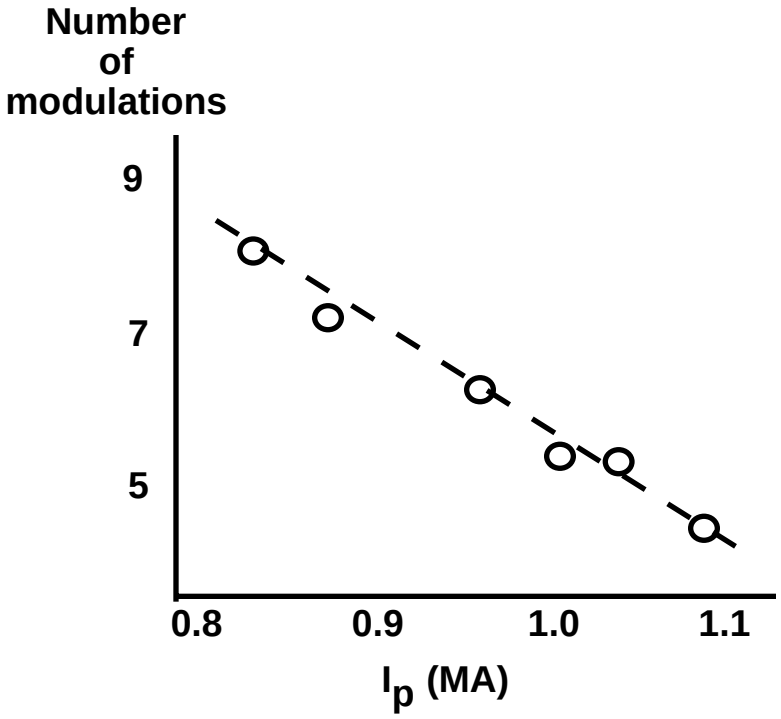

Figure 5

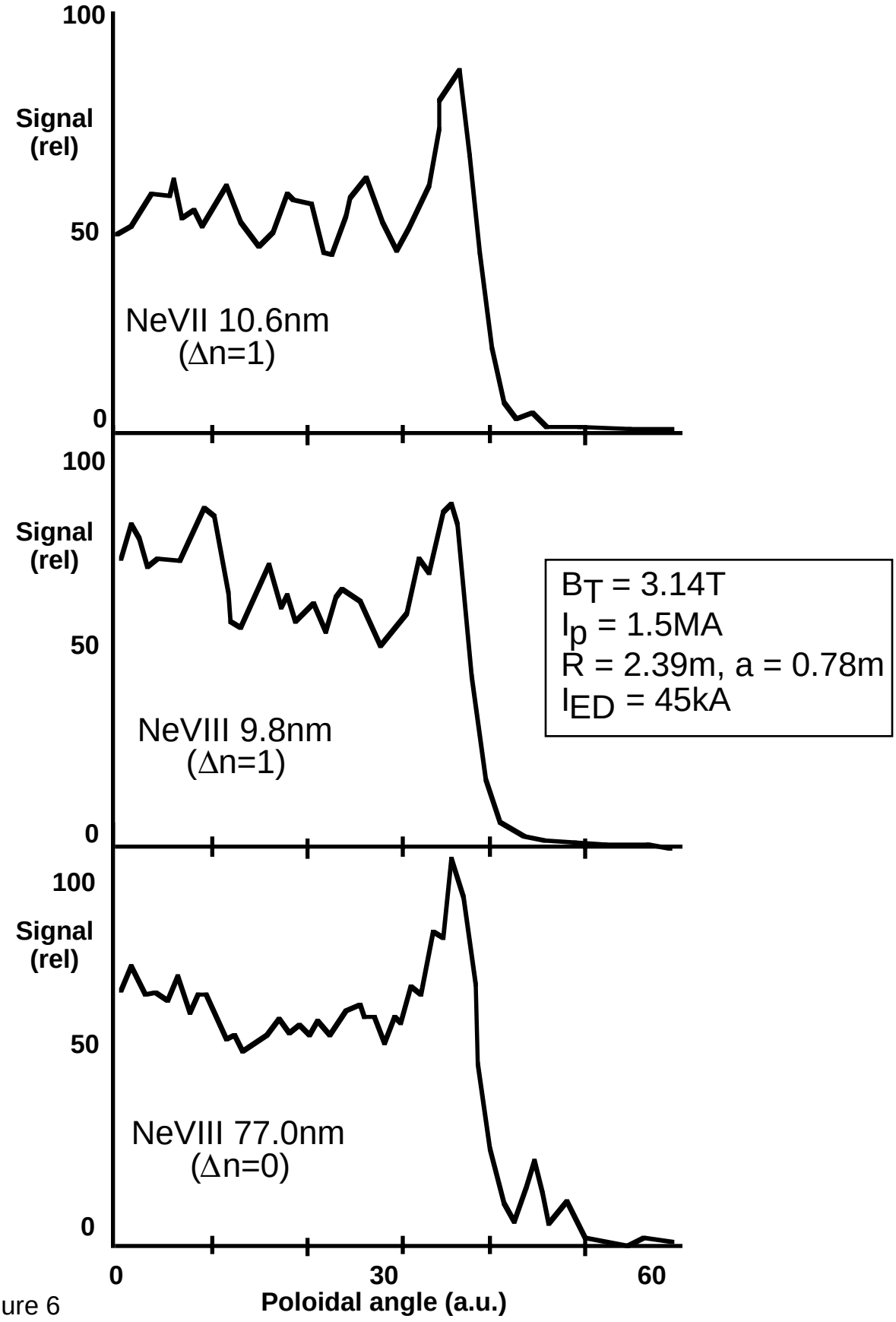
100
Signal
(rel)
50
0
NeVII 10.6nm
(Δn=1)
100
Signal
(rel)
50
0
NeVIII 9.8nm
(Δn=1)
B_T = 3.14T
I_p = 1.5MA
R = 2.39m, a = 0.78m
I_{ED} = 45kA
100
Signal
(rel)
50
0
NeVIII 77.0nm
(Δn=0)
0
30
60
Poloidal angle (a.u.)

Figure 6

Typical map: distribution of ρ_{min} on the boundary surface of the BBQ solution volume

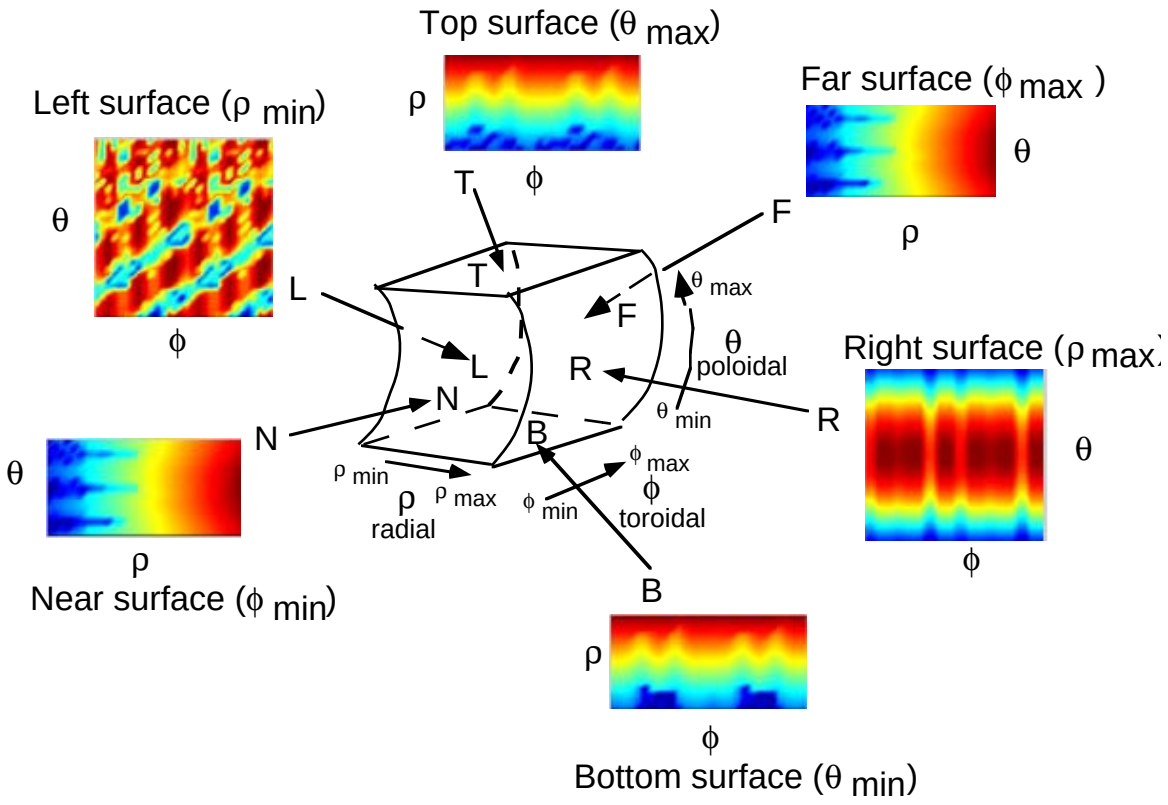

Figure 7

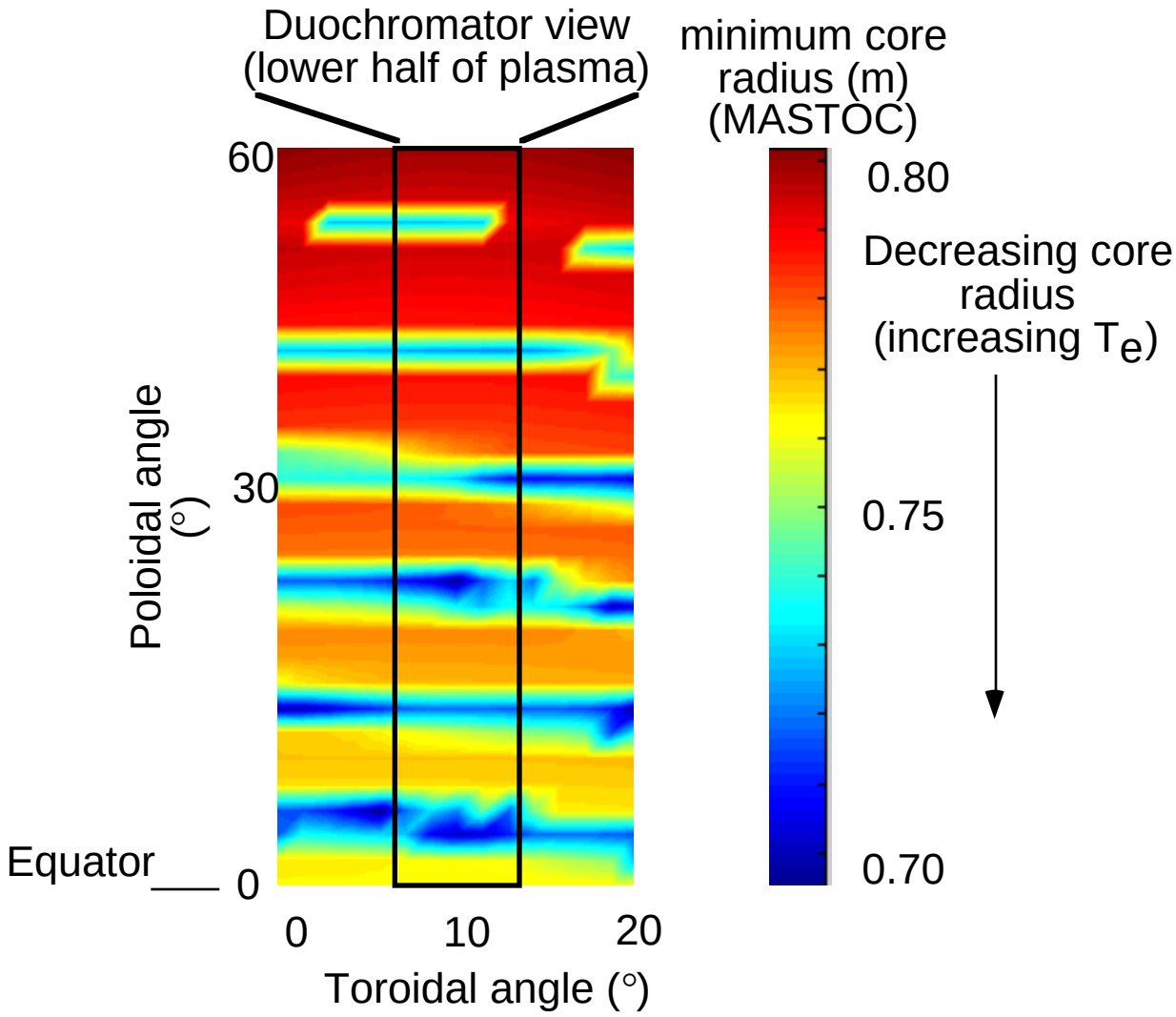
Duochromator view
(lower half of plasma)
minimum core
radius (m)
(MASTOC)
60
30
0
Poloidal angle
(°)
Equator
0
10
20
Toroidal angle (°)
0.80
0.75
0.70
Decreasing core
radius
(increasing T_e)

Figure 8

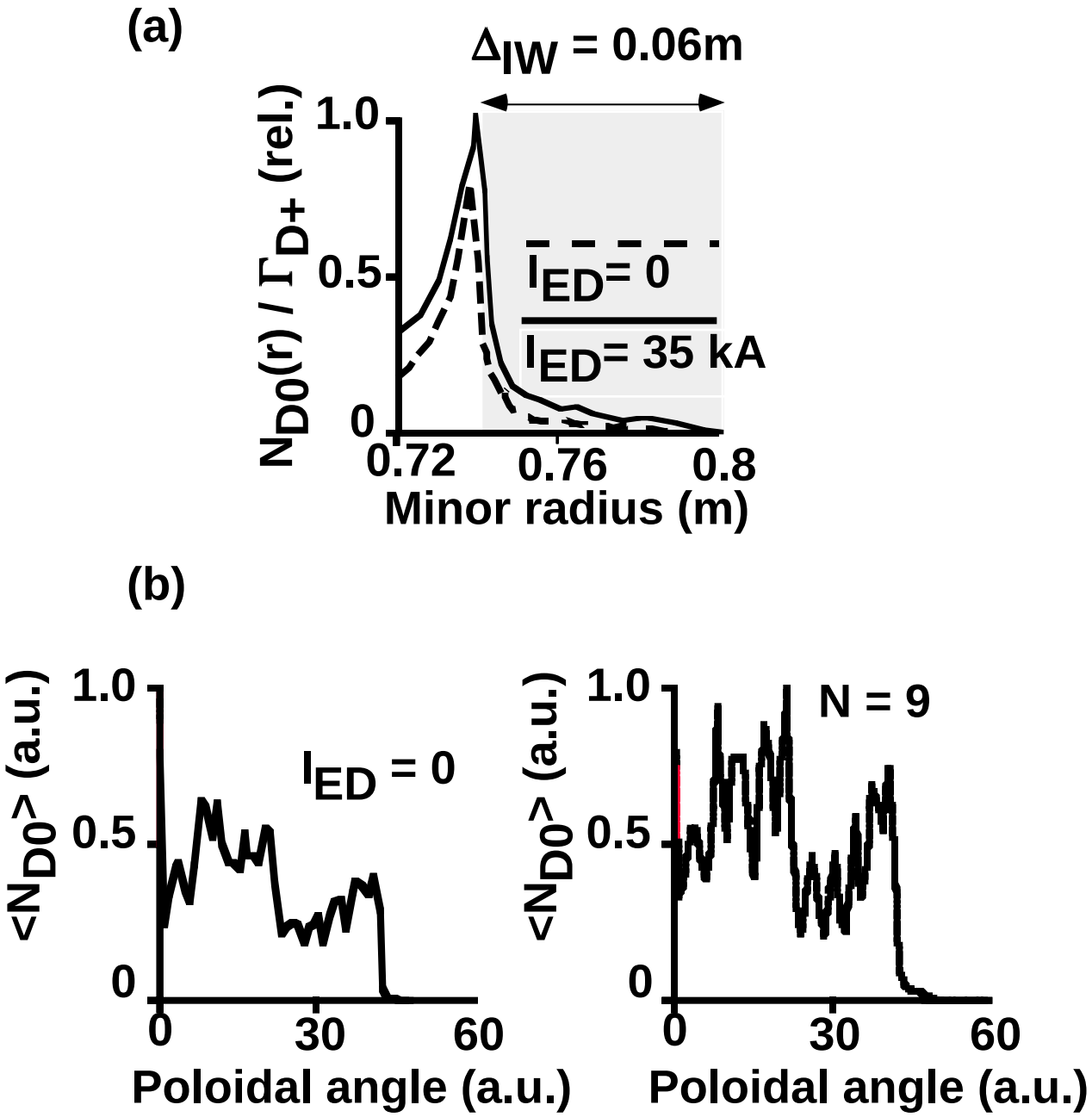
(a)
Δ_{IW} = 0.06m
1.0
0.5
0
$N_{D0}(r) / \Gamma_{D+}$ (rel.)
I_{ED}= 0
I_{ED}= 35 kA
0.72
0.76
0.8
Minor radius (m)
(b)
1.0
0.5
0
<N_{D0}> (a.u.)
I_{ED} = 0
0
30
60
Poloidal angle (a.u.)
1.0
0.5
0
<N_{D0}> (a.u.)
N = 9
0
30
60
Poloidal angle (a.u.)

Figure 9

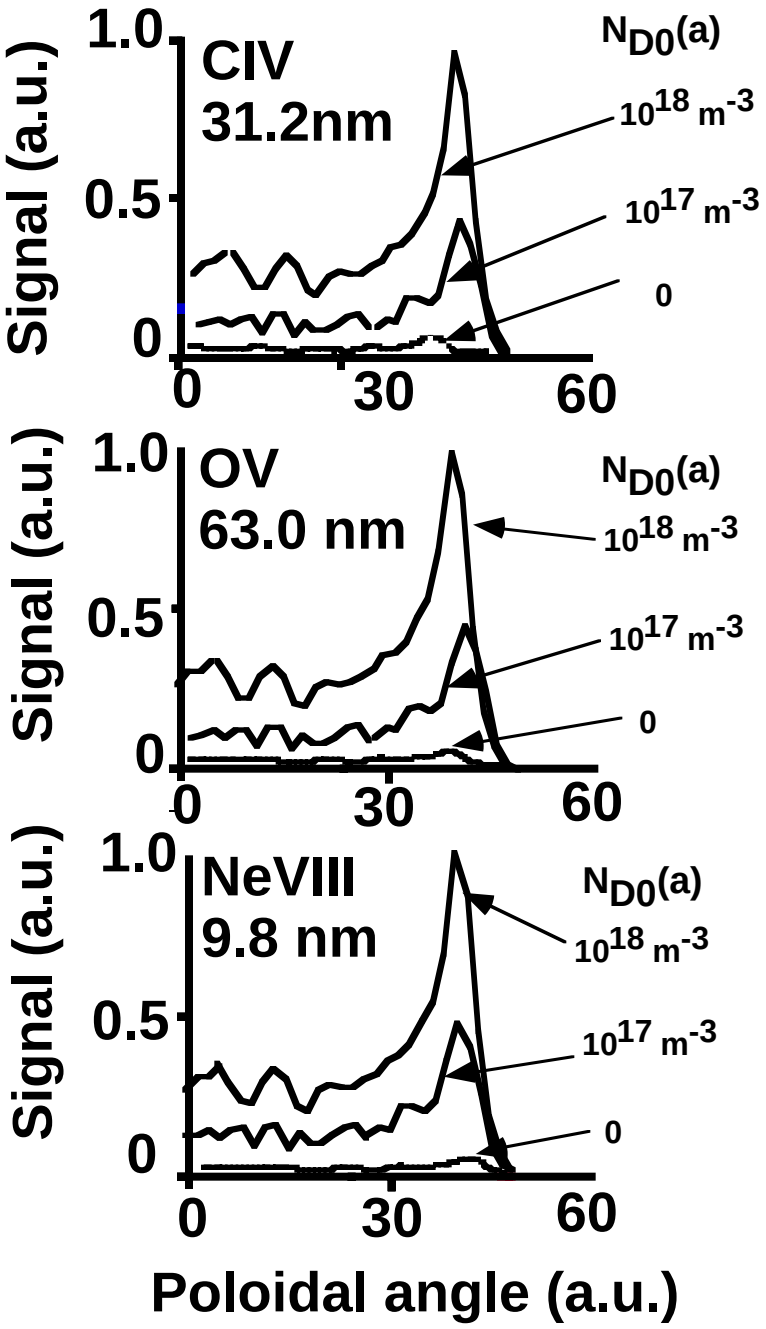
CIV
31.2nm
OV
63.0 nm
NeVIII
9.8 nm
Signal (a.u.)
1.0
0.5
0
0
30
60
$N_{D0}(a)$
10^{18} m^{-3}
10^{17} m^{-3}
0
Poloidal angle (a.u.)

Figure 10

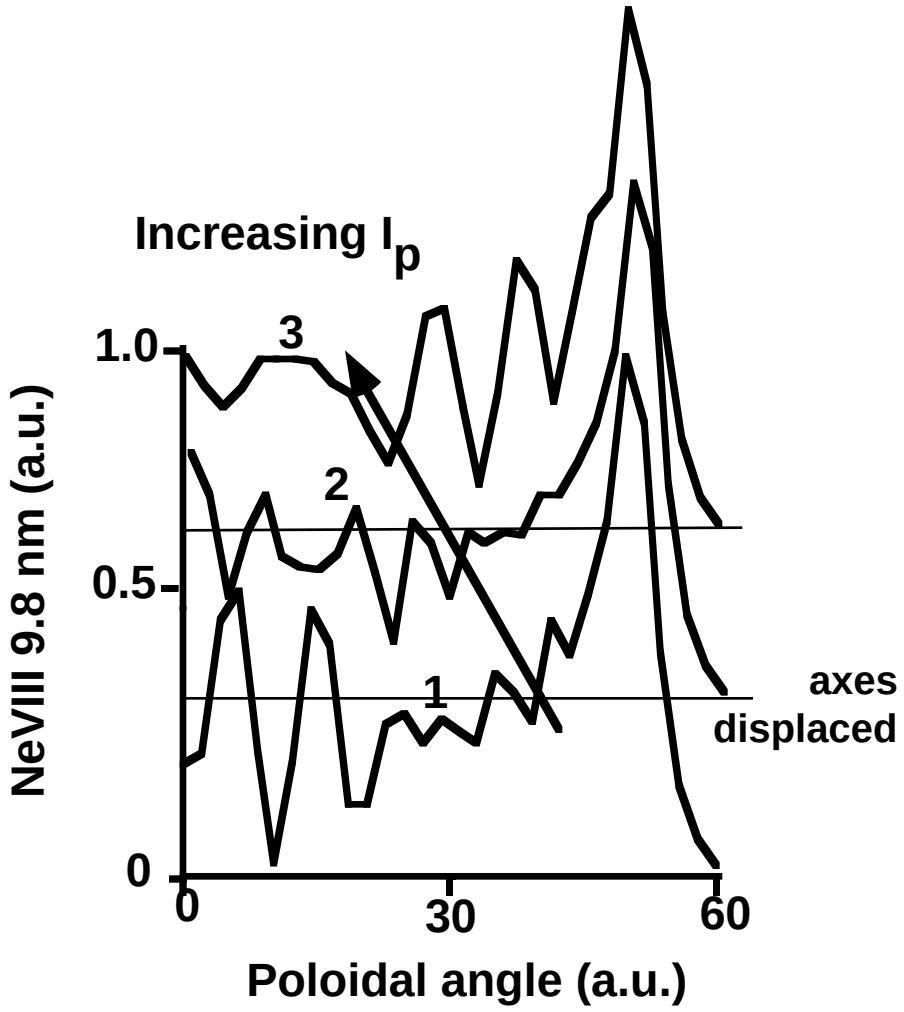
Increasing I_p
1.0
0.5
0
3
2
1
axes
displaced
NeVIII 9.8 nm (a.u.)
0
30
60
Poloidal angle (a.u.)

Figure 11